Vacancy-Induced Semiconductor−Insulator−Metal Transitions in Nonstoichiometric Nickel and Tungsten Oxides

Qi Wang,[†] Ajinkya Puntambekar,[†] and Vidhya Chakrapani[*,†,‡]

[†]Howard P. Isermann Department of Chemical and Biological Engineering and [‡]Department of Physics, Applied Physics, and Astronomy, Rensselaer Polytechnic Institute, Troy, New York 12180, United States

Ⓢ Supporting Information

ABSTRACT: Metal−insulator transitions in strongly correlated oxides induced by electrochemical charging have been attributed to formation of vacancy defects. However, the role of native defects in affecting these transitions is not clear. Here, we report a new type of phase transition in p-type, nonstoichiometric nickel oxide involving a semiconductor-to-insulator-to-metal transition along with the complete reversal of conductivity from p- to n-type at room temperature induced by electrochemical charging in a Li^+-containing electrolyte. Direct observation of vacancy-ion interactions using in situ near-infrared photoluminescence spectroscopy show that the transition is a result of passivation of native nickel (cationic) vacancy defects and subsequent formation of oxygen (anionic) vacancy defects driven by Li^+ insertion into the lattice. Changes in the oxidation states of nickel due to defect interactions probed by X-ray photoemission spectroscopy support the above conclusions. In contrast, n-type, nonstoichiometric tungsten oxide shows only insulator-to-metal transition, which is a result of oxygen vacancy formation. The defect-property correlations shown here in these model systems can be extended to other oxides.

KEYWORDS: Nickel oxide, metal-to-insulator transition, Li^+ insertion, vacancy defects, electronic structure
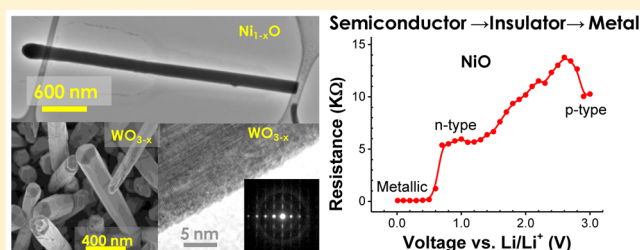
Metal−insulator transitions (MIT) have attracted significant research in the past decade in a number of strongly correlated, undoped and doped transition metal oxides such as nickelates, manganites, and vanadates.[1−11] The transitions between the insulating and metallic phases can be induced by different types of external stimuli, such as temperature, strain,[2] pressure,[3,4] electron doping,[1] chemical doping,[5,6] magnetic field,[7] disorder,[8] and light.[9−11] In addition, electrochemical charging (or gating) has been used to suppress and induce phase transitions, which has been attributed to both electrostatic charge injection[12] and to the formation of vacancy defects during gating of VO_2 in ionic liquid.[13,14] In most of these studies, the gating of channel conductance was achieved through electrostatic charging at the semiconductor/ionic liquid interface without involving faradaic reactions. Although the formation of vacancy defects during charging has been attributed a role in the phase transition process, the role played by native defects formed during growth in the MIT process is not clear. Here, we report a new type of room-temperature phase transition, involving semiconductor-to-insulator-to-metal transition (SIMT) seen in strongly correlated, p-type, nonstoichiometric nickel oxide ($Ni_{1−x}O$) that is induced by the interaction of native vacancy defects with redox species such as Li^+ during electrochemical charging. Li^+ insertion into $Ni_{1−x}O$ causes a change in the conductivity from p- to n-type, which was reported by Passerini and Bruno and attributed to electron doping.[15] In this study, we show that the type of vacancy defects and nature of vacancy-ion interaction primarily

determines the nature of MIT transitions during electrochemical charging. Nonstoichiometric $Ni_{1−x}O$, which is p-type due to the presence of cationic vacancies, shows SIMT as result of passivation of native cationic (nickel) vacancy defects by Li^+ and subsequent formation of anionic (oxygen) defects during charging. These vacancy-ion interactions lead to the complete reversal of electronic conductivity from p- to n-type, as seen by Passerini and Bruno.[15] In contrast to SMIT in $Ni_{1−x}O$, nonstoichiometric tungsten oxide ($WO_{3−x}$), which is n-type due to the presence of oxygen vacancy defects in the lattice, shows an insulator-to-metal transition that occurs as a result of formation of more oxygen vacancies in the lattice.

Vacancies in transition metal oxides (TMOs) have been probed using a number of spectroscopic techniques, such as scanning tunneling microscopy (STM),[16−20] electron energy loss spectroscopy (EELS),[21,22] X-ray absorption measurements,[23,24] and ultraviolet or X-ray photoemission spectroscopy (XPS).[25,26] As one of the most powerful experimental techniques for studying surface atomic processes, STM has revealed various defects existing on oxide surfaces with high spatial resolution, thereby contributing to a deeper understanding of the role of defects in adsorbate binding and dissociation. Although STM affords a magnificent atomic-level visualization of binding of adsorbed species on defect sites, it
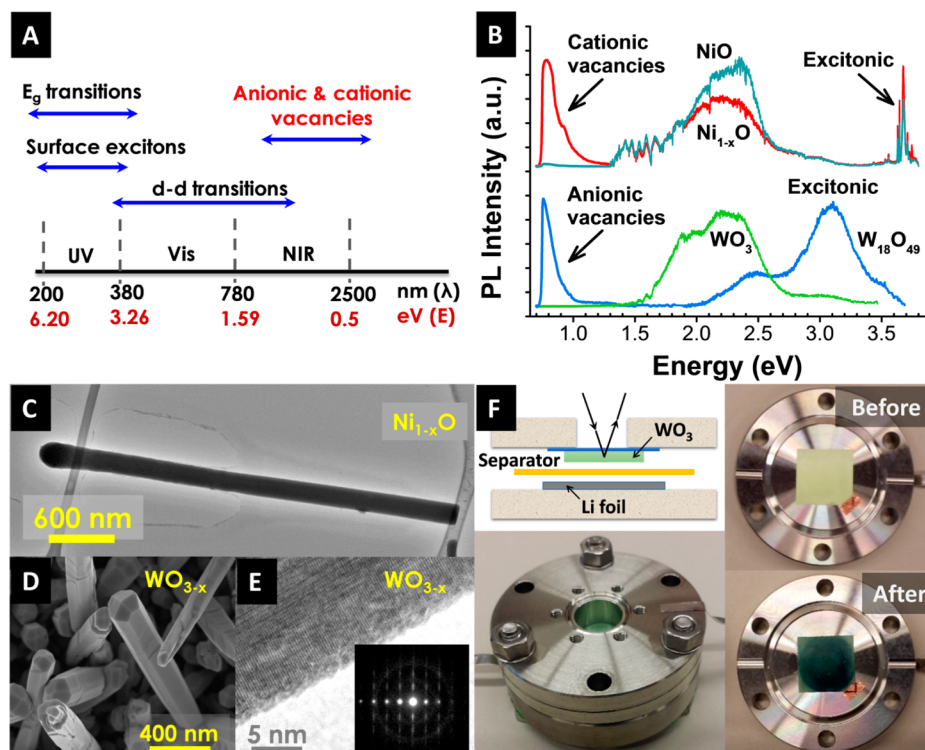
Figure 1. (A) Energy range of the various radiative transitions in transition metal oxides spanning from UV to NIR spectral region. (B) Photoluminescence spectra of nonstoichiometric ($Ni_{1-x}O$) and stoichiometric (NiO) nickel oxide as well as stoichiometric (WO_3) and nonstoichiometric ($W_{18}O_{49}$) tungsten oxide. Presence of vacancy defects in nonstoichiometric oxides gives rise to a NIR emission peak at 0.7−0.8 eV that is absent in stoichiometric oxides. (C) TEM of $Ni_{1-x}O$ nanowires. (D) Scanning electron micrograph of $W_{18}O_{49}$ nanowires. (E) HRTEM image of a single crystal of $W_{18}O_{49}$. Inset: corresponding selected area diffraction pattern showing streak lines corresponding to oxygen vacancy in the (600) plane. (F) Schematic and photographs of the electrochemical cell used for in situ PL measurements. Also shown is the WO_3 sample before and after intercalation with Li^+ ions.

gives little information about the molecular structure or the nature of electronic interaction between the defects and adsorbates. Furthermore, STM, along with other methods such as EELS and XPS, requires carefully prepared single crystal surfaces in an ultrahigh-vacuum environment. Although some studies have been done under high-pressure conditions,[27−29] these techniques are difficult to adapt to electrochemical studies that involve reactive environments, the presence of metal catalysts, and sometimes samples with a high density of existing defects. Clearly, no single experimental approach can encompass the complexity inherent in probing structural and electronic changes during electrochemical processes. Instead, a number of different optical and electron spectroscopy probes must be applied and their results correlated. Here, we use near-infrared photoluminescence (NIR-PL) spectroscopy for studying vacancy defects in metal oxides and their interaction with redox species under in-operando electrochemical cell conditions. The advantages of PL spectroscopy are that it can be highly surface-sensitive and is a nondestructive method that can be easily adapted with minimum surface preparation for in situ catalytic studies that may involve the presence of a metal catalyst (<5 wt %), thin water films, or reactive gas environments.

The spectral range of radiative emissions seen in TMOs is shown in Figure 1A. Many TMOs are strongly ionic, and hence have band-to-band or excitonic emissions that lie in the UV-to-visible spectral region. If the oxide is nonstoichiometric, it results in the changes in the oxidation state of the metal center, the occupancy of d-band, and formation of new electronic states within the band gap. Most d−d transitions, which occur between the electronic levels of incompletely filled "d" orbitals, give rise to PL emission in the visible range, while both cationic and anionic vacancies have emissions in the near-infrared (NIR) spectral region. For instance, representative PL spectra of stoichiometric and nonstoichiometric nickel and tungsten oxides are shown in Figure 1B. In nonstoichiometric nickel oxide ($Ni_{1-x}O$), both excitonic and free-carrier emission occurs at ~3.8 eV. Nonstoichiometry in NiO predominately results in a high density of metal (cationic) vacancies that gives rise to an NIR-PL emission at ~0.8 eV. In contrast, the stoichiometric oxide (NiO) shows no NIR emission. Similarly, in nonstoichiometric tungsten oxide (WO_{3-x}), the predominant defects are oxygen (anionic) vacancy defects that also gives rise to midgap electronic states within the band gap and a PL emission centered at ~0.75 eV, while the stoichiometric oxide (WO_3) shows no NIR emission. (The exact nature of electronic transitions giving rise to these NIR emissions is discussed in the latter sections of this paper.) This defect-induced NIR emission provides a direct tool for probing vacancy-ion interactions during electrochemical charging.

Nanostructures of tungsten and nickel oxide were synthesized by hot filament chemical vapor deposition (HFCVD) technique, which involves resistively heating W or Ni metal wire close to its melting point in the presence of either pure oxygen or a mixture of argon, oxygen, and water vapor. The reaction of oxygen with the hot metal filament results in the formation of the respective metal oxide on the substrates placed under the filament. Morphology and stoichiometry of the
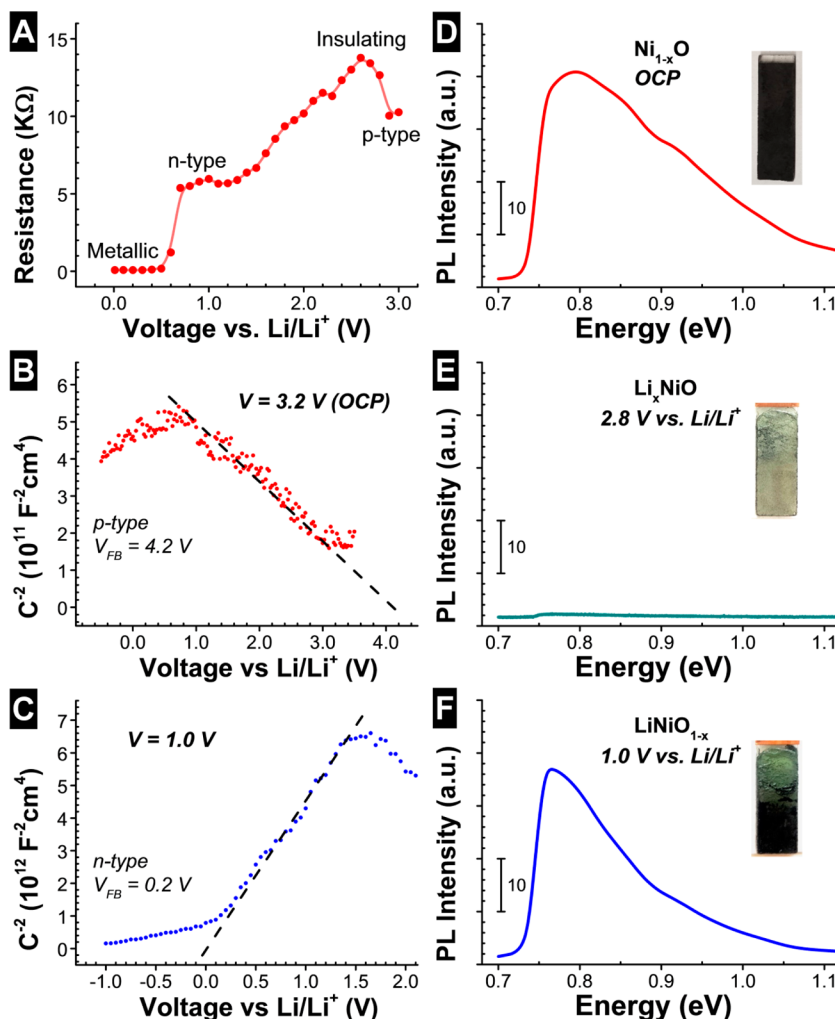
Figure 2. (A) Changes in the two-probe electrical resistance of $Ni_{1-x}O$ showing a semiconductor-to-insulator-to-metal transition during electrochemical reduction in 0.1 M $LiClO_4$ in propylene carbonate. (B,C) In situ Mott−Schottky plots of $Ni_{1-x}O$ at 3.2 V (B) and 1.0 V (C) in an electrolyte solution consisting of 0.1 M TBAP in propylene carbonate. (D−F) Changes in the intensity of NIR emissions as a result of Li^+ insertion into the lattice of (D) as-synthesized, nonstoichiometric NiO ($Ni_{1-x}O$) containing Ni vacancies. Inset: photograph of $Ni_{1-x}O$ coated ITO electrode. (E) Li^+ passivated insulating NiO (Li_xNiO) charged to a potential of 2.8 V. Inset: photograph of Li_xNiO electrode. (F) Heavily Li^+ intercalated NiO ($LiNiO_{1-x}$) charged to a potential of 1.0 V. Inset: photograph of $LiNiO_{1-x}$ electrode.

deposited sample can be modulated by tuning the filament power and oxygen partial pressure in the chamber. Nanowires with a range of metal-to-oxygen ratios can be prepared with high purity using this technique without introducing extraneous reducing agents, as shown in our recent work.[30,31] In addition to the nanostructures prepared using HFCVD, nonstoichiometric, single crystal nickel oxide nanowires and nanoparticles were also purchased from Sigma-Aldrich. Electrochemical measurements showed no significant differences in the observed trend between nanoparticles, nanowires, or thin films. Nickel oxide nanowires used in this study had a diameter of ~100 nm and were 1−2 μm in length, as seen in the transmission electron microscopy (TEM) image shown in Figure 1C and the scanning electron micrographs (SEM) shown in Figure.S1 in the Supporting Information (SI). X-ray diffraction (XRD) patterns of both stoichiometric and nonstoichiometric oxides, shown in Figure.S2 in SI, conform to the JCPDS pattern of cubic NiO. SEM images of both stoichiometric and nonstoichiometric tungsten oxide nanowires show them to be aligned nanowires of 5−6 μm in length with a diameter of 60−80 nm. Representative images are shown in

Figure 1D and Figure.S3 in SI. The X-ray diffraction pattern of the nonstoichiometric phase shows the crystal structure to be monoclinic $W_{18}O_{49}$ ($WO_{2.72}$), which is shown in Figure.S4 in SI. High-resolution TEM (HRTEM) images of $W_{18}O_{49}$ show sequential bright and dark contrast fringes throughout the length of the wire, indicating a single crystalline nature (see Figure 1E and Figure.S3C). Distinct in-plane vacancy ordering in the direction parallel to the nanowire growth direction can be observed to be the predominant defect in nonstoichiometric oxide, which can be seen as an ordered white-spot array in the lattice-resolved TEM image (Figure 1E and Figure.S3C in the SI) taken along the [010] direction. The streak lines in the selected area electron diffraction (SAED) pattern (inset in Figure 1E and Figure.S3D) and the visible planar defect structure parallel to the growth direction is attributed to oxygen vacancies, V_O in the (600) plane, which is consistent with prior TEM studies on $W_{18}O_{49}$ nanowires grown under similar conditions.[32] The lattice fringe distances, 0.38 and 0.28 nm, were consistent with d-spacings of (010) and (600), and the SAED pattern was in conformity to the [001] zone axis of the monoclinic $W_{18}O_{49}$ phase.

To probe the nature of defect-ion interaction and its effect on electronic properties, changes in the NIR-PL, two-probe electrical resistance, and electrochemical Mott−Schottky (capacitance versus voltage) measurements were performed in situ at various stages (or potentials) of Li$^+$ ion intercalation. Changes in the sample resistance at different electrochemical bias were correlated with the observed changes in the intensity of NIR emission, and in turn with the density of defect states. In addition, ex situ X-ray photoelectron spectroscopy (XPS) measurements were done on lithiated samples, and the results were correlated with the results of in situ electrochemical Mott−Schottky and NIR-PL measurements. Figure 1F shows the schematic and photographs of the electrochemical cell used for in situ PL measurements. Metal oxide nanowires grown on indium tin oxide-coated glass substrates were sandwiched with a Li metal foil along with a fiberglass separator soaked with the electrolyte containing 0.1 M LiClO$_4$ in propylene carbonate. A stainless steel electrochemical cell was built with an optical window that enabled in situ measurements. PL measurements were done by optically probing the sandwiched electrode, which was pressed against the optical window from the backside. Electrochemical charging was done by applying a constant potential step and allowing the electrode to reach equilibrium, which was until the charging current reached a minimum value. The charging was then interrupted and the two-probe electrical resistance of the sample was measured between two separate molybdenum contacts placed on the sample. Electrochemical Mott−Schottky measurements were done at various stages of charging to ascertain the nature of uncompensated majority charge carriers. Measurements were done by interrupting the charging process in the Li$^+$ electrolyte and transferring the electrode to a different cell with the electrolyte consisting of 0.1 M tertiary butyl ammonium perchlorate (TBAP) in propylene carbonate and Li metal serving as the reference and counter electrode. From the measured capacitance (C), a plot of C^{-2} versus potential (V) was constructed. The nature of charge carriers was ascertained from the slope of this curve. All potentials in the text are referred with respect to a Li/Li$^+$ reference electrode that has a standard electrode potential of −3.05 V versus standard hydrogen electrode.[33] Figure 1F shows the photographs of a WO$_3$ electrode before and after intercalation of Li$^+$ ions. Representative results of NiO and WO$_3$ are summarized in Figure 2 and Figure 5, respectively.

The evolution of two-probe electrical resistance of Ni$_{1−x}$O during electrochemical charging is shown in Figure 2A. Application of a reduction potential between 3.2 V (open-circuit potential, OCP) and 0.5 V results in injection of e$^-$ and Li$^+$ into the lattice. The insertion of Li$^+$ into Ni$_{1−x}$O results in complex changes in the resistivity leading to a SIMT and a change in the polarity of electrical conduction from p-type to n-type. Mott−Schottky analysis of as-synthesized Ni$_{1−x}$O is shown in Figure 2B. The negative slope of the curve indicates that the majority charge carriers are holes and that the conductivity is p-type. Extrapolation of the linear portion of the curve to the abscissa gives the value of flat band potential (Fermi level), E_{FB}, which for Ni$_{1−x}$O at OCP was determined to be 4.2 V versus Li/Li$^+$. The color of a pristine sample was greenish-black. An optical image of the sample is shown in the inset of Figure 2D. Upon electrochemical charging, the resistance of Ni$_{1−x}$O first increases with an increase in Li$^+$ concentration in the lattice starting from 3.2 V and reaches a maximum at ∼2.8 V. At the maximum resistance, the sample turns white (see inset of Figure 2E) and the material behaves as an insulator (denoted as Li$_x$NiO). This change in the coloration from black to white is consistent with the prior observation of electrochromism in NiO.[34−36] A further increase in the Li$^+$ concentration of the sample leads to a decrease in the sample resistance, which was accompanied by a switch in the polarity of electrical conduction from p- to n-type, as seen by the change in the slope of the Mott−Schottky plot (shown in Figure 2C) from negative to positive. This change in the conductivity from p- to n-type at high Li$^+$ concentration is consistent with the shifts in the photocurrent responses observed by Passerini and Bruno.[15] The flat band potential of lithiated oxide (denoted as LiNiO$_{1−x}$) charged to 1.0 V was estimated to be 0.2 V versus Li/Li$^+$. This shift in the value of flat band potential of nearly 4.0 V between p-type and n-type oxide phases is equal to the band gap of NiO, which has been reported in the range of 3.6−4.0 eV. The color of the n-type sample (LiNiO$_{1−x}$) turns from white to bluish-black (see inset of Figure 2F). At potentials below 0.8 V versus Li/Li$^+$, progressive Li$^+$ intercalation renders the sample metallic. Thus, unlike in other correlated oxides, such as VO$_2$, where application of reduction potential induces the metallic phase and suppresses the insulating phase, in Ni$_{1−x}$O, charging induces first the insulating phase at lower reduction potentials and then a metallic phase at higher reduction potentials.

MIT transition in VO$_2$ and in other correlated oxides, such as NdNiO$_3$, La$_{0.8}$Sr$_{0.2}$MnO$_3$ in ionic liquid electrolyte has been attributed to the formation of oxygen vacancy defects that stabilizes the metallic phase.[13,37,14,38,39] To understand the role of vacancy defects in the observed SIMT in Ni$_{1−x}$O, we performed in situ NIR-PL measurements at various stages of electrochemical charging. NiO is one of the easily reducible oxides, and irradiation with high energy UV or electron probe beams during measurements can easily cause oxygen desorption from the lattice. To avoid forming V$_O$ defects during PL measurements, spectra in the NIR region were taken using a sub-band gap He−Ne laser at an excitation wavelength of 633 nm. No observable difference was seen in the NIR spectra between spectra taken using excitation laser of 325 or 633 nm wavelength. Snapshots of the PL spectra recorded in the NIR spectral range of the p-type semiconducting, insulating, and metallic phases of Ni$_{1−x}$O, which corresponds to oxide phases obtained at potentials of 3.2 (OCP), 2.8, and 1.0 V, respectively, are shown in Figure 2D−F. The spectrum of Ni$_{1−x}$O at OCP shows a broad band luminescence centered near 0.8 eV (Figure 2D). Electrochemical reduction at 2.8 V, which corresponds to the potential of maximum electrical resistance, results in a complete quenching of the 0.8 eV emission peak, which is indicative of complete passivation of defects responsible for the 0.8 eV emission peak by Li$^+$ ions (Figure 2E). This spectrum at 2.8 V appears similar to the spectrum of stoichiometric NiO in the NIR range shown in Figure 1B. At a more negative potential of 1.0 V, a new emission peak centered at ∼0.75 eV appears (Figure 2F). All changes in the PL and electrical resistance were completely reversible, that is, out diffusion of Li$^+$ results in the recovery of the ground state corresponding to a pristine sample. For instance, the quenching of the PL signal seen at 2.8 V can be recovered by exposure of the cell to room air, which is shown in Figure.S5 in SI. This results in the recovery of the NIR emission intensity to the value obtained from a pristine nonstoichiometric oxide before electrochemical reduction. The inset in the figure shows the kinetic trace of the emission
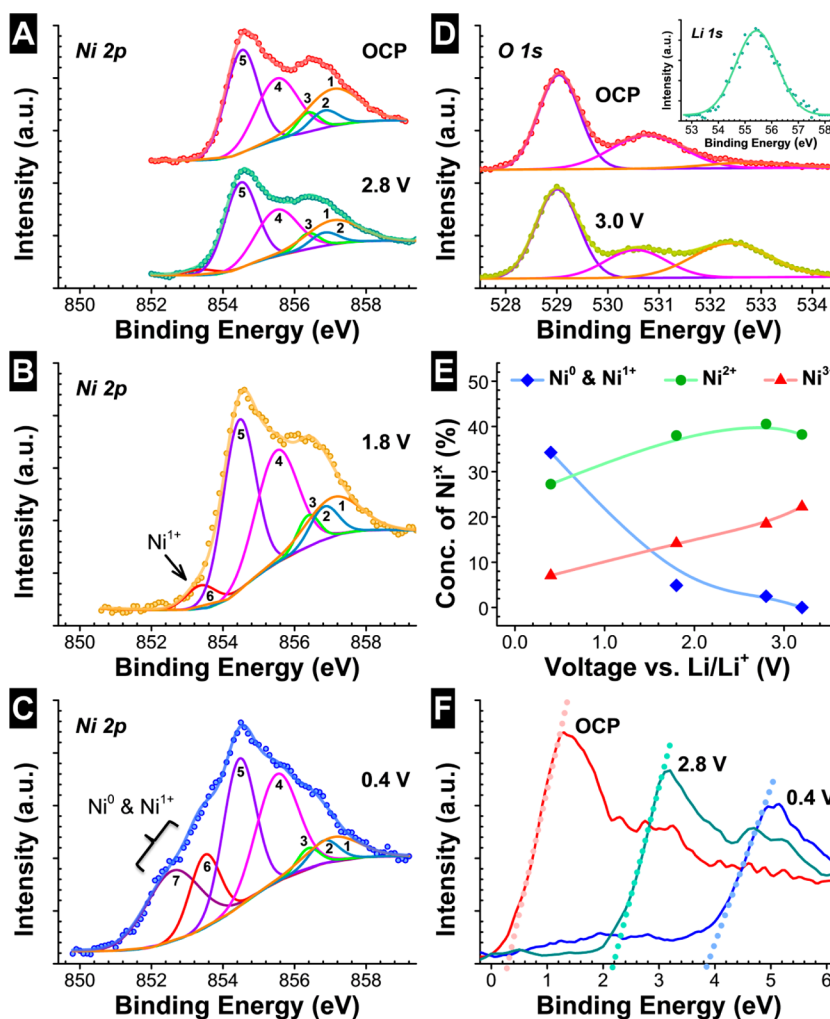
Figure 3. (A−C) XPS spectra of the Ni $2p_{3/2}$ core level before and after Li$^+$ insertion at potential of 2.8, 1.8, and 0.4 V and fitted with Ni^{2+} and Ni^{3+} multiplet envelops predicted by Gupta and Sen.[44,45] The summary of the fitting analysis of the labeled peaks and their peak energy positions, areas, and FWHMs is given in Table S2 in SI. Comparison of the curves shows the broadening of the Ni $2p_{3/2}$ peak toward the lower BE with progressive reduction. This peak broadening, which is most evident in the spectra of samples charged to 1.8 and 0.4 V, is due to the formation of Ni^0 and Ni^{1+}. In addition, the intensity of peak at higher binding energy of 857.1 eV, which is due to Ni^{3+}, decreases with increasing reduction potentials. (D) Changes in the O 1s spectra of samples charged at 3.2 (OCP) and 3.0 V. Inset: XPS spectrum of Li 1s of sample charged to 2.8 V. (E) The relative changes in the concentration of Ni^0, Ni^{1+}, Ni^{2+}, and Ni^{3+}, as estimated from the XPS analysis, in the samples during electrochemical charging. (F) Changes in the low-binding-energy valence spectra between samples charged at OCP, 2.8 and 0.4 V. The intercept of the flat line to the abscissa gives the value of $E_F−E_V$, which for Ni$_{1−x}$O increases to a higher value with increases in the Li$^+$ concentration in the crystal.

recovery monitored at $E = 0.78$ eV. From the NIR-PL results, it is clear that the semiconductor-to-insulator transition seen between 3.2 to 2.8 V is a result of passivation of native defects in Ni$_{1−x}$O by Li$^+$ insertion. It is known that Ni$_{1−x}$O is inherently a p-type semiconductor with a propensity for formation of high density of Ni$^+$ vacancies, V$_{Ni}$, and excess oxygen interstitial atoms during growth that renders the crystal nonstoichiometric.[15,40] As seen in Figure 1B, the presence of these native defects gives rise to a NIR-PL with a peak centered at ~0.8 eV. The inherent p-type conductivity of the oxide suggests that V$_{Ni}$ gives rise to acceptor type states that are located ~0.8 eV above the valence band maximum (VBM). Passivation of V$_{Ni}$ defects or interstitial oxygen by Li$^+$ leads to the quenching of p-type conductivity and formation of an insulating phase with relatively few or no vacancy defect states, which may explain the lack of PL signal in the NIR spectral range. The insulator-to-metal transition occurring at higher Li$^+$ concentrations (between 2.8 to 0.5 V biases) may be a result of

formation of new type of defect states. Since, the Mott− Schottky results indicate that the conductivity is n-type at a high Li$^+$ concentration, the newly formed states would most likely be donor-type states. From the peak position in NIR-PL, we infer that these donor-type states have an electronic energy ~0.75 eV below the energetic position of conduction band minimum (CBM). It is clear that there is a correlation between evolution of resistance changes seen during SIMT and passivation and formation of various types of defects in the crystal lattice as a result of ion intercalation.

To identify the nature of the defect states responsible for SIMT as well as the chemical nature of the compositional changes, ex situ XPS was done to observe the changes in the oxidation state of Ni$_{1−x}$O at various stages of electrochemical charging. Samples for XPS were prepared by interrupting the charging process at various potentials. Electrodes were emmersed from the electrolyte, rinsed with propylene carbonate to remove superficial impurities, dried, and trans-

ferred to the XPS chamber immediately to minimize air exposure. Figure 3A−C compares the Ni $2p_{3/2}$ core-level spectrum obtained from a pristine (as-synthesized) sample to the spectra from samples after electrochemical charging at potentials that gives rise to the insulating (2.8 V), n-type semiconducting (1.8 V), and metallic (0.4 V) phases of lithiated oxide. Energy shifts due to residual charging were corrected with respect to peak position of adventitious carbon at a binding energy (BE) of 284.8 eV. Several prior XPS studies on nickel oxide have pointed out the complex nature of the BE spectra of Ni and the analysis involved in the interpretation of the peaks.[41−43] Complexities arise due to the peak broadening, multiplet splitting of the main Ni 2p emission peak, and formation of broad satellite peaks at BE of ∼6 eV from the main line that are a result of electrostatic interactions and spin−orbit coupling between 2p hole and unpaired 3d electrons of the photoionized cation, as suggested by Gupta and Sen.[44,45] In addition to the Ni 2p peak, the change in the oxidation state of Ni is also reflected in the O 1s peak, where the presence of Ni^{3+} in the lattice gives rise to an additional peak in the O 1s emission line.[43,15] Differences in the bonding of oxygen with Ni^{3+} compared to Ni^{2+} give rise to a secondary peak in the O 1s spectra at BE of 531.7 eV in addition to the main peak at 529.9 eV corresponding to O 1s of Ni^{2+}−O bonding, as seen in Figure 3D. However, a quantitative description of changes in the compositional ratio of Ni^{2+}/Ni^{3+} in the film during charging using the O 1s peak was not possible because of the additional influence of newly formed oxygen-containing compounds such as Li_2O, C=O species that give rise to new shoulder peak at the BE of 532.4 eV in the O 1s spectra. The concentration of various elements and hence the stoichiometry of the film can be derived from the relative integrated peak areas of main emission lines of respective elements corrected for the sensitivity factors, provided the film is homogeneous. The nanostructured nature of NiO in the present study prevented the evaluation of film stoichiometry. Nevertheless, from the integrated peak areas of Ni $2p_{3/2}$ and O 1s, the stoichiometry of pristine NiO was estimated to be 2.16, which indicates oxygen enrichment in the nonstoichiometric oxide. Given the approximate nature of this value, no further analysis was done. Instead, the ratio of Ni^{2+}/Ni^{3+} in the film was estimated from the contribution of both oxidation states to peak areas of the Ni $2p_{3/2}$ emission line, which was insensitive to sample inhomogeneity.

The Ni $2p_{3/2}$ peak was fit using peaks constrained to conform to the multiplet envelopes calculated by Gupta and Sen (GS),[44,45] and McIntyre and co-workers[41] for NiO. To calculate the peak areas, the background from each spectrum was subtracted using a Shirley-type correction to remove extrinsic loss structure. The GS-predicted multiplet peaks of Ni $2p_{3/2}$ envelop for free Ni^{2+} and Ni^{3+} ions are shown in Figure.S6 and summarized in Table S1 in SI.[41] The spectra of $Ni_{1−x}O$ at various potentials were fitted with both Ni^{2+} and Ni^{3+} envelops using peaks whose full width at half-maximum (FWHM) was in range of 0.72 to 1.74 eV. Fitting was done by constraining both the energetic positions as well as the FWHM of the peaks to the same values between spectra recorded at various charging potentials. In addition to the GS-multiplet peaks, two additional peaks corresponding to Ni^0 at the BE of 852.6 eV[41,46] and Ni^{1+} at the BE of 853.4 eV[46] were added to complete the fit for samples that were electrochemically charged. The summary of the fitting analysis showing the peak positions, areas, and FWHMs of Ni $2p_{3/2}$ peak fitted with GS multiplet peaks is given in Table S2 in SI. Comparison of

the spectra shown in Figure 3A−C taken at potentials 2.8, 1.8, and 0.4 V with the spectrum of pristine sample at OCP resulted in the following observations: (i) with progressive reduction, there is a broadening of the Ni $2p_{3/2}$ peak toward the lower BE, which is most evident in the spectra of 1.8 and 0.4 V when the sample shows n-type conductivity. This peak broadening is due to the formation of nickel of lower oxidation states, such as Ni^0 and Ni^{1+}. New peaks at the lower BE of 852.6 and 853.4 eV is consistent with previous reports on the BE of Ni^0 and Ni^{1+} atoms.[42,46] Spectra of n-type semiconducting $Ni_{1−x}O$ that was charged to 1.8 V shows an increase in the Ni^{1+} signal, while the metallic $Ni_{1−x}O$ at 0.4 V has strong contributions from both Ni^0 and Ni^{1+}. (ii) With progressive lithiation, the intensity of main peak corresponding to Ni^{3+}, which appears at the higher BE of 857.1 eV, decreases. Accurate determination of the concentrations of Ni^{3+} and Ni^{2+} was hampered by the presence of overlapping peaks for Ni^{2+} and Ni^{3+}, which is evident from the GS multiplet peak for free Ni^{2+} and Ni^{3+} ions shown in Figure.S6. As pointed out by McIntyre and co-workers,[41] although it is difficult to assign a single BE to either Ni^{2+} or Ni^{3+}, the predominant peaks of Ni^{3+} appear at the higher BE (857.1 eV) from the main emission line at 854.5 eV.[41] To calculate the relative changes in the concentration of Ni^{3+}, the integrated area of the Gaussian curve with peak at the BE of 857.1 eV was used, which has singular contribution from Ni^{3+}. The concentration of Ni^{2+} was estimated from the curve with the peak intensity at the BE of 854.5 eV. The relative changes in the concentration of Ni^0, Ni^{1+}, Ni^{2+}, and Ni^{3+}, as estimated from the XPS analysis, in the samples during electrochemical charging is shown in Figure 3E. Between OCP and 2.8 V, which marks the transition from a p-type semiconducting phase to an insulating phase, the concentration of Ni^{3+} decreases, while concentration of Ni^{2+} increases. This points to the conversion of Ni^{3+} to Ni^{2+}. The maximum in the concentration of Ni^{2+} occurs at a potential of 2.8 V when the $Ni_{1−x}O$ is insulating and stoichiometric. The decrease in the Ni^{2+} concentration below 2.8 V indicates progressive conversion of Ni^{2+} to lower oxidation states of Ni^{1+} and Ni^0, which coincides with the switch in the conductivity to n-type. The inset in the Figure 3D shows the Li 1s spectra of the oxide lithiated at 2.8 V. The BE of the peak at 55.6 eV occurs at the same position as the peak for Li_2O reported in the XPS database.

The valence band XPS spectra at the low BE gives information about shifts in the Fermi energy. The intercept to the abscissa of a straight line fitted to the rising portion of the valence band edge curve gives the value of $E_F−E_V$. Figure 3F shows the valence band spectra of $Ni_{1−x}O$ in the low BE range at various electrochemical potentials. As can be seen, the value of $E_F−E_V$ progressively increases with increasing lithiation. The $E_F−E_V = 0.3$ eV for pristine $Ni_{1−x}O$ is consistent with a p-type conduction resulting from holes in the valence band, as confirmed by Mott−Schottky measurements (Figure 2B). At a potential of 2.8 V, the $E_F−E_V$ was determined to be 2.2 eV, which is nearly half the value of the band gap of 3.8 eV, indicating that the Fermi energy is at the midgap and the material behaves as an insulator. At a potential of 0.4 V, there is a clear shift of $E_F−E_V$ to a larger value of 3.8 eV, indicating that the Fermi level is closer to the CBM. The sample is n-type, which is consistent with the result of Mott−Schottky analysis (Figure 2C) and the results of Passerini and Bruno.[15]

The changes in the electrical resistance and electrochemical properties can be understood by considering the band structure of $Ni_{1−x}O$ along with the data from the NIR-PL and XPS
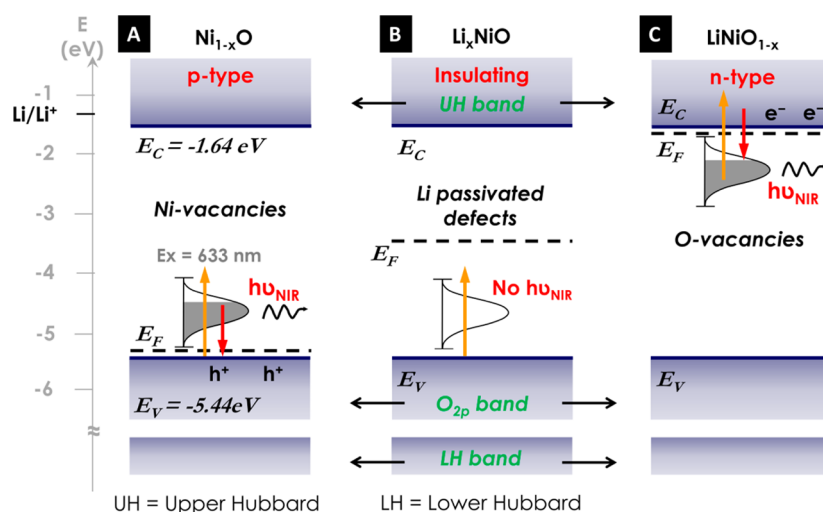
Figure 4. Schematic of energy band diagrams of (A) nonstoichiometric $Ni_{1-x}O$ containing Ni vacancies, (B) Li^+ passivated insulating NiO (Li_xNiO) at a potential of 2.8 V, (C) Heavily Li^+ intercalated n-type NiO ($LiNiO_{1-x}$) at a potential below 2.8 V, showing the midgap energy states and the various radiative transitions resulting from the formation and passivation of vacancies.
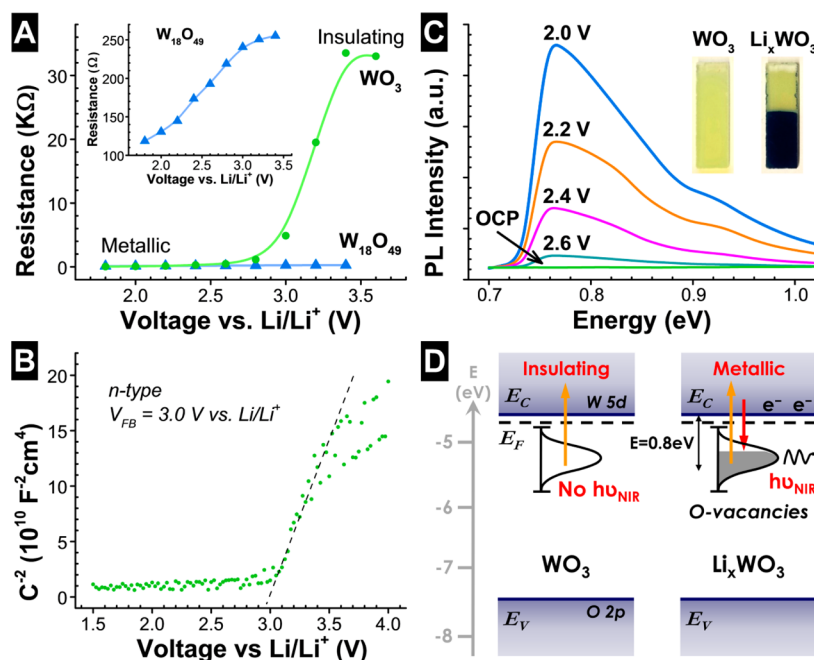

Figure 5. (A) Changes in the two-probe resistance of WO_3 and $W_{18}O_{49}$ leading to an insulator-to-metal transition occurring during electrochemical reduction in a Li^+-containing electrolyte. Inset: Expanded view of the resistance changes during Li^+ insertion into $W_{18}O_{49}$. (B) Mott−Schottky analysis of WO_3 showing n-type behavior with a flat band potential (V_{FB}) of 3.0 V vs the Li/Li^+ reference electrode. (C) Rise in the intensity of NIR emission as a result of Li^+ insertion into the lattice at various electrochemical potentials. Inset: photographs of WO_3 and Li^+ intercalated WO_3 (Li_xWO_3) electrodes. (D) Schematic of the energy band diagrams of WO_3 and Li_xWO_3 showing the midgap energy states and the various radiative transitions resulting from the formation of oxygen vacancies.

measurements. Unlike many TMOs, NiO represents an important class of materials whose band structures show marked deviations from the predictions of ligand field theory as a result of strong electron−electron correlations.[47] According to the Mott−Hubbard model,[48,49] NiO is a charge transfer insulator. Strong repulsion between electrons in the narrow Ni d-band causes splitting of the d-band into upper and lower Hubbard bands and a significant amount of hybridization between Ni 3d and O 2p states. In stoichiometric oxide, the band gap transition is a result of excitation between the highest occupied valence band, which although it is hybridized, shows primarily the O 2p character, and the lowest unoccupied

conduction band, which is the upper Hubbard band with Ni 3d character. The lower Hubbard band is a filled band and lies below the occupied O 2p band. In nonstoichiometric nickel oxide, deviation in stoichiometry is due to the presence of V_{Ni}, and interstitial oxygen.[40,43] Each V_{Ni} leads to formation of two holes to obtain charge neutrality, which results in the change in the oxidation state of two neighboring nickel atoms to Ni^{3+}. Schematic of energy band diagrams of $Ni_{1-x}O$ and the various types of radiative transitions occurring with sub-band gap excitation resulting from passivation and formation of defect states is shown in Figure 4. The presence of Ni^{3+} (or V_{Ni}), as confirmed by XPS, gives rise to acceptor-type midgap defect

states closer to the VBM and imparts a p-type character to the oxide, as shown in the schematic in Figure 4A. Electronic transitions between V_{Ni} defect states and VBM result in the NIR emission peak at ~0.8 eV seen in nonstoichiometric NiO (Figure 2D). This energy difference of 0.8 eV seen in PL measurements is consistent with the value of 0.8 eV reported for coulomb interaction between double charge vacancy and a d-hole in nonstoichiometric nickel oxide.[50] During electrochemical charging at potentials between OCP and 2.8 V, insertion and binding of Li^+ may occur at the interstitial O^{2-} sites, which will cause passivation of V_{Ni} defects (see Figure 4B). This should lead to a decrease in the concentration of Ni^{3+} and a corresponding increase in the Ni^{2+} concentration, which was confirmed from the XPS results shown in Figure 3D. In the present study, the charge density required to achieve the passivated state at a potential of 2.8 V was ~12 mC/cm². The passivation of V_{Ni} defects and excess interstitial oxygen renders the crystal stoichiometric. The material behaves as a wide band gap insulator with its Fermi level at the midgap. Passivation also leads to a complete quenching of NIR emission (Figure 2E) and a change in the optical coloration of the sample from black to white. This quenching of V_{Ni} defect states may be responsible for the prior reports on the electrochromic effect[51,35] in NiO, where the transmittance of the sample is known to increase with small increases in the Li^+ concentration in the crystal. Further insertion of Li^+ into the stoichiometric crystal at potentials more negative than 2.8 V causes binding of inserted Li^+ at the O^{2-} lattice sites and makes it nonstoichiometric with the resulting formation of V_O defects (Figure 4C). The presence of V_O defects will result in the lowering of the oxidation state of neighboring nickel atoms from Ni^{2+} to Ni^0 or Ni^{1+}, which is evident in the XPS spectra of $Ni_{1-x}O$ charged at 0.4 and 1.8 V. Because V_O defects are usually donor-type states in metal oxides, it leads to the creation of midgap states closer to the CBM of NiO that imparts n-type characteristics. The NIR emission peak seen at 0.75 eV is probably a result of electron transitions between these donor-type states and the CBM. The color of the sample changes from white to bluish black, as shown in the inset of Figure 3F. The electrical conduction in the crystal becomes metallic with any further insertion of Li^+ ions in NiO.

Li^+ insertion into p-type $Ni_{1-x}O$ results in SIM transition. To explore the effect of Li^+ in an n-type oxide, we chose tungsten oxides (WO_3 and $W_{18}O_{49}$) as the model systems. Both $W_{18}O_{49}$ and nominally undoped WO_3 are n-type due to the presence of oxygen vacancies, V_O, in the lattice formed during growth. The effect of Li^+ insertion on electrical resistance and NIR emission was tested and the results are summarized in Figure 5. In contrast to the effect seen in p-type $Ni_{1-x}O$, electrochemical charging of both WO_3 and $W_{18}O_{49}$ leads to a steady decrease in electrical resistance that renders the sample metallic, as shown in Figure 5A. The stoichiometric oxide (WO_3) exhibits a dramatic insulator-to-metal transition. Whereas, the nonstoichiometric phase ($W_{18}O_{49}$), which is highly conducting even in its pristine state, shows a smaller drop in the electrical resistance, as shown in the expanded scale in the Inset in Figure 5A. Stoichiometric tungsten oxide is light green in optical coloration with no detectable NIR emission, while nonstoichiometric phase showed dark blue coloration and a strong NIR emission due to the presence of oxygen vacancy (V_O) planes, as described earlier in this text. Electrochemical reduction of the stoichiometric oxide causes a strong NIR emission peak to appear, centered at ~0.76 eV. The intensity of

this peak increases with progressive Li^+ intercalation into the oxide, as shown in Figure 5C.

According to the ligand field theory,[52] the conduction band of WO_3 is derived mainly from the metal d-states, and the valence band is composed primarily of O 2p states. In stoichiometric form, the d-band of tungsten oxide is empty, and the material remains an insulator. The main radiative transitions seen in the stoichiometric oxide are the band gap or excitonic transitions with no NIR defect-related transitions, as shown in Figure 1B. In nonstoichiometric tungsten oxide, $W_{18}O_{49}$, the presence of V_O defects generates a high density of midgap electronic states closer to the CBM, thus making the oxide an n-type semiconductor. The NIR emission shown in Figure 1B from $W_{18}O_{49}$ is a result of the transition from the conduction band edge to the V_O defect states. Similarly, intercalation of Li^+ ions into stoichiometric WO_3 results in an increase in n-type conductivity, as confirmed by Mott–Schottky measurements shown in Figure 5B. The color of sample turns from light green to dark blue upon Li^+ intercalation, as seen in Figure 5C and 1F. The binding of Li^+ ions with lattice O^{2-} sites results in the formation of V_O defect sites and changes in the oxidation state of neighboring tungsten atoms from W^{6+} to W^{5+} and W^{4+}.[53] The insulator-to-metal transition is due to the increasing density of oxygen vacancy formation. From the energetic position of the NIR emission peak of both $W_{18}O_{49}$ and Li_xWO_3, it can be concluded that V_O midgap states are located ~0.76 eV below the conduction band edge. The change in the color of the sample from green to blue may be due to the presence of filled electronic midgap states below the conduction band edge that causes light absorption in the most of the visible range except in the blue spectral range between 3 to 2.5 eV, where the electron transitions from the valence band to the filled midgap states is precluded due to the state-filling. The change in the absorption spectra as a result of Li^+ into WO_3 is shown in Figure.S7 in SI. Figure 5D shows a schematic diagram of the band structure and the type of radiative transitions occurring with sub-band gap excitation in WO_3 and Li_xWO_3.

In conclusion, metal−insulator transitions in metal oxide induced by electrochemical charging are driven by formation and annihilation of vacancy defects. In nonstoichiometric NiO, in situ NIR-PL measurements show that Li^+ and e^- injection result in a semiconductor−insulator−metal transition that is caused by the passivation of cationic (nickel) vacancies formed during growth and the formation of new anionic (oxygen) vacancies during charging. In contrast, both nonstoichiometric and stoichiometric tungsten oxide show only an insulator−metal transition upon Li^+ insertion due to the formation of oxygen vacancy defects. Understanding defect-ion interactions is crucial for elucidating structure−property correlations underlying many functional oxides. For instance, TMOs are a technologically important class of materials that are valued for their catalytic, ferroelectric, and optical properties. They have a wide range of applications in heterogeneous catalysis, photocatalysis, sensors, solar cells, fuel cells, and batteries. The highly catalytic nature of the oxide in these applications is due to the rich surface chemistries enabled by the interaction of gases and ions with lattice defects. Ion insertion has been shown to have a profound impact on the optical and electrical properties of many two-dimensional host systems. For instances, recent studies have demonstrated that metallic Cu insertion into Bi_2Se_3 leads to significant enhancement of light transmission properties and electrical conductivity.[54] Similar effects on optical properties have been noted in other materials, such as

ultrathin graphite[55] and MoS_2[56] layers with Li^+ insertion, which is contrary to the decrease in optical transmittance observed in WO_3 in this study. These varying effects of chemical or ion doping on the optical properties emphasizes the need to understand the underlying electronic structural changes resulting from chemical interactions. The results shown here provide an example on how defect-ion interaction can lead to profound changes in the electronic, electrical, and optical properties of metal oxides that can directly influence functional catalytic properties.

Methods and Materials. *Nanostructure Synthesis.* WO_3 and NiO nanowires were synthesized by hot filament chemical vapor deposition on indium tin oxide (ITO) coated glass that served as the conductive back contact. The technique involves resistively heating W or Ni metal wire close to its melting point in the presence of feed gases consisting of either pure oxygen or a mixture of argon, oxygen, and water vapor at partial pressures ranging from 0.1 to 10 Torr. The reaction of oxygen with the hot metal filament results in the formation of the respective metal oxide nanostructure on the substrates placed under the filaments. Both the morphology and stoichiometry of the deposited sample could be modulated by tuning the filament power, chamber pressure, and oxygen partial pressure in the chamber. Oxides with a range of metal-to-oxygen stoichiometry could be prepared with high purity using this technique without the introduction of extraneous reducing agents. More details can be found in our prior publication.[30]

Material Characterization. The composition and structure of the as-synthesized metal oxides were characterized by X-ray diffraction. Morphology of the samples was examined by both SEM and TEM. As-deposited NiO films on a glass substrate were analyzed and confirmed by XRD. HFCVD samples were crystalline cubic phase of NiO. The observed 2θ peaks at 37.3, 43.3, 62.9, 75.4, and 79.4 are in good agreement with JCPDS data file (no. 01-071-1179) of (111), (200), (220), (311), and (222) reflections. PL measurements in the range from 330 to 1700 nm were obtained using a HORIBA Scientific LabRAM HR Evolution spectrometer equipped with Si and InGaAs charge-coupled device detectors using an excitation wavelength of 325 nm (He−Cd laser) and 633 nm (He−Ne laser). All PL spectra were obtained at room temperature in a reflective backside configuration. Absorption spectra in the spectral range of 220−3000 nm were recorded using Shimadzu 3600 UV−vis-NIR spectrophotometer.

XPS measurements were done using a Physical Electronics PHI 5000 Versa Probe system comprising of a monochromatic $Al(K_\alpha)$ (1486.7 eV) X-ray source and a 150 mm radius hemispherical electron energy analyzer. The analyzer was operated at pass energies between 11.75 and 29.35 eV, and at a chamber base pressure of $\sim 10^{-10}$ Torr.

Electrochemical Testing. Lithium ion intercalation of $Ni_{1-x}O$, WO_3, and $W_{18}O_{49}$ was performed in a standard three-electrode electrochemical cell configuration with Li metal as both the counter and reference electrodes in a nonaqueous electrolyte consisting of 0.1 M $LiClO_4$ in propylene carbonate. Electrochemical charging was done by applying a constant potential step using a Zahner IM6 electrochemical workstation and allowing the electrode to reach equilibrium, which was until the charging current reached a minimum value. A sample charging curve is shown in Figure.S8 in the SI. It was observed that the time for complete charging of the sample at a given applied potential, which corresponds to the time it takes to completely intercalate the entire nanowire/nanoparticle film

with Li^+ to obtain state of uniform charge, was dependent on the thickness of the electrode film and the applied potential. Thinner film had a smaller equilibration time versus thicker film. The injected charge to obtain the oxygen deficient phase of WO_3 was approximately 30 mC/cm^2. A charge of 12 mC/cm^2 was used to obtain nearly stoichiometric NiO (Li_xNiO), and 30 mC/cm^2 was injected to obtain a heavily Li^+ intercalated, oxygen deficient NiO ($LiNiO_{1-x}$). Mott−Schottky analysis was used to determine the flat band potentials and the type of majority charge carriers under various stages of Li^+ intercalation using a Li metal foil as the counter and reference electrodes in 0.1 M TBAP in propylene carbonate. All electrical and electrochemical measurements were carried out in an argon atmosphere glovebox.

Electrical Measurements. In situ two-probe resistance measurements was done at various stages of electrochemical charging using two molybdenum sample clips placed approximately 1 cm apart on the surface of the samples. At each step potential value, the intercalation process was allowed to reach equilibrium (0.5−2 h). This process was then interrupted to measure the sample resistance.

■ ASSOCIATED CONTENT

ⓢ Supporting Information

The Supporting Information is available free of charge on the ACS Publications website at DOI: 10.1021/acs.nano-lett.6b03311.

SEM, TEM, XRD patterns, and detailed XPS analysis of the data reported in the text (PDF)

■ AUTHOR INFORMATION

Corresponding Author

*E-mail: chakrv@rpi.edu.

Notes

The authors declare no competing financial interest.

■ ACKNOWLEDGMENTS

■ REFERENCES

(1) Shi, J.; Zhou, Y.; Ramanathan, S. Colossal resistance switching and band gap modulation in a perovskite nickelate by electron doping. *Nat. Commun.* **2014**, *5*, 4860.

(2) Aetukuri, N. B.; Gray, A. X.; Drouard, M.; Cossale, M.; Gao, L.; Reid, A. H.; Kukreja, R.; Ohldag, H.; Jenkins, C. A.; Arenholz, E.; Roche, K. P.; Durr, H. A.; Samant, M. G.; Parkin, S. S. P. Control of the metal-insulator transition in vanadium dioxide by modifying orbital occupancy. *Nat. Phys.* **2013**, *9* (10), 661−666.

(3) Loa, I.; Adler, P.; Grzechnik, A.; Syassen, K.; Schwarz, U.; Hanfland, M.; Rozenberg, G. K.; Gorodetsky, P.; Pasternak, M. P. Pressure-Induced Quenching of the Jahn-Teller Distortion and Insulator-to-Metal Transition in $LaMnO_3$. *Phys. Rev. Lett.* **2001**, *87* (12), 125501.

(4) Arcangeletti, E.; Baldassarre, L.; Di Castro, D.; Lupi, S.; Malavasi, L.; Marini, C.; Perucchi, A.; Postorino, P. Evidence of a Pressure-Induced Metallization Process in Monoclinic VO_2. *Phys. Rev. Lett.* **2007**, *98* (19), 196406.

(5) Byon, J. W.; Kim, M.-B.; Kim, M. H.; Kim, S. Y.; Lee, S. H.; Lee, B. C.; Baik, J. M. Electrothermally Induced Highly Responsive and Highly Selective Vanadium Oxide Hydrogen Sensor Based on Metal−Insulator Transition. *J. Phys. Chem. C* **2012**, *116* (1), 226−230.

(6) Boebinger, G. S.; Ando, Y.; Passner, A.; Kimura, T.; Okuya, M.; Shimoyama, J.; Kishio, K.; Tamasaku, K.; Ichikawa, N.; Uchida, S. Insulator-to-Metal Crossover in the Normal State of La$_{2-x}$Sr$_x$CuO$_4$ Near Optimum Doping. *Phys. Rev. Lett.* **1996**, *77* (27), 5417−5420.

(7) Kuwahara, H.; Tomioka, Y.; Asamitsu, A.; Moritomo, Y.; Tokura, Y. A first-order phase transition induced by a magnetic field. *Science* **1995**, *270* (5238), 961.

(8) Motome, Y.; Furukawa, N.; Nagaosa, N. Competing Orders and Disorder-Induced Insulator to Metal Transition in Manganites. *Phys. Rev. Lett.* **2003**, *91* (16), 167204.

(9) Ohkoshi, S.-i.; Tsunobuchi, Y.; Matsuda, T.; Hashimoto, K.; Namai, A.; Hakoe, F.; Tokoro, H. Synthesis of a metal oxide with a room-temperature photoreversible phase transition. *Nat. Chem.* **2010**, *2* (7), 539−545.

(10) Wu, J. M.; Liou, L. B. Room temperature photo-induced phase transitions of VO$_2$ nanodevices. *J. Mater. Chem.* **2011**, *21* (14), 5499−5504.

(11) Lysenko, S.; Rúa, A.; Vikhnin, V.; Fernández, F.; Liu, H. Insulator-to-metal phase transition and recovery processes in VO$_2$ thin films after femtosecond laser excitation. *Phys. Rev. B: Condens. Matter Mater. Phys.* **2007**, *76* (3), 035104.

(12) Bubel, S.; Hauser, A. J.; Glaudell, A. M.; Mates, T. E.; Stemmer, S.; Chabinyc, M. L. The electrochemical impact on electrostatic modulation of the metal-insulator transition in nickelates. *Appl. Phys. Lett.* **2015**, *106* (12), 122102.

(13) Jeong, J.; Aetukuri, N.; Graf, T.; Schladt, T. D.; Samant, M. G.; Parkin, S. S. P. Suppression of Metal-Insulator Transition in VO$_2$ by Electric Field−Induced Oxygen Vacancy Formation. *Science* **2013**, *339* (6126), 1402−1405.

(14) Singh, S.; Abtew, T. A.; Horrocks, G.; Kilcoyne, C.; Marley, P. M.; Stabile, A. A.; Banerjee, S.; Zhang, P.; Sambandamurthy, G. Selective electrochemical reactivity of rutile VO$_2$ towards the suppression of metal-insulator transition. *Phys. Rev. B: Condens. Matter Mater. Phys.* **2016**, *93* (12), 125132.

(15) Passerini, S.; Scrosati, B. Characterization of nonstoichiometric nickel oxide thin-film electrodes. *J. Electrochem. Soc.* **1994**, *141* (4), 889−895.

(16) Bikondoa, O.; Pang, C. L.; Ithnin, R.; Muryn, C. A.; Onishi, H.; Thornton, G. Direct visualization of defect-mediated dissociation of water on TiO$_2$ (110). *Nat. Mater.* **2006**, *5* (3), 189−192.

(17) Bonnell, D. A. Scanning tunneling microscopy and spectroscopy of oxide surfaces. *Prog. Surf. Sci.* **1998**, *57* (3), 187−252.

(18) Diebold, U. Intrinsic defects on a TiO$_2$(110) surface and their reaction with oxygen: A scanning tunneling microscopy study. *J. Vac. Sci. Technol., A* **1998**, *411*, 137−153.

(19) Schaub, R. Oxygen-mediated diffusion of oxygen vacancies on the TiO2(110) surface. *Science* **2003**, *299*, 377−379.

(20) Wendt, S.; Sprunger, P. T.; Lira, E.; Madsen, G. K. H.; Li, Z.; Hansen, J. Ø.; Matthiesen, J.; Blekinge-Rasmussen, A.; Lægsgaard, E.; Hammer, B.; Besenbacher, F. The Role of Interstitial Sites in the Ti3d Defect State in the Band Gap of Titania. *Science* **2008**, *320* (5884), 1755−1759.

(21) Wang, Z. L.; Yin, J. S.; Jiang, Y. D. EELS analysis of cation valence states and oxygen vacancies in magnetic oxides. *Micron* **2000**, *31* (5), 571−580.

(22) Rocker, G.; Schaefer, J. A.; Göpel, W. Localized and delocalized vibrations on TiO$_2$ (110) studied by high-resolution electron-energy-loss spectroscopy. *Phys. Rev. B: Condens. Matter Mater. Phys.* **1984**, *30* (7), 3704−3708.

(23) Anspoks, A.; Kalinko, A.; Kalendarev, R.; Kuzmin, A. Probing vacancies in NiO nanoparticles by EXAFS and molecular dynamics simulations. *J. Phys.: Conf. Ser.* **2013**, *430* (1), 012027.

(24) Ariza, M. J.; Jones, D. J.; Rozière, J.; Chitrakar, R.; Ooi, K. Probing the Local Structure and the Role of Protons in Lithium Sorption Processes of a New Lithium-Rich Manganese Oxide. *Chem. Mater.* **2006**, *18* (7), 1885−1890.

(25) Henrich, V. E.; Dresselhaus, G.; Zeiger, H. J. Observation of Two-Dimensional Phases Associated with Defect States on the Surface of TiO$_2$. *Phys. Rev. Lett.* **1976**, *36* (22), 1335−1339.

(26) Schulze, M.; Reissner, R.; Lorenz, M.; Radke, U.; Schnurnberger, W. Photoelectron study of electrochemically oxidized nickel and water adsorption on defined NiO surface layers. *Electrochim. Acta* **1999**, *44* (23), 3969−3976.

(27) Longwitz, S. R.; Schnadt, J.; Vestergaard, E. K.; Vang, R. T.; Stensgaard, I.; Brune, H.; Besenbacher, F. High-Coverage Structures of Carbon Monoxide Adsorbed on Pt(111) Studied by High-Pressure Scanning Tunneling Microscopy†. *J. Phys. Chem. B* **2004**, *108* (38), 14497−14502.

(28) van Spronsen, M. A.; van Baarle, G. J. C.; Herbschleb, C. T.; Frenken, J. W. M.; Groot, I. M. N. High-pressure operando STM studies giving insight in CO oxidation and NO reduction over Pt(1 1 0). *Catal. Today* **2015**, *244*, 85−95.

(29) Zhu, Z.; Tao, F. F.; Zheng, F.; Chang, R.; Li, Y.; Heinke, L.; Liu, Z.; Salmeron, M.; Somorjai, G. A. Formation of nanometer-sized surface platinum oxide clusters on a stepped Pt(557) single crystal surface induced by oxygen: a high-pressure STM and ambient-pressure XPS study. *Nano Lett.* **2012**, *12* (3), 1491−7.

(30) Chakrapani, V.; Brier, M.; Puntambekar, A.; DiGiovanni, T. Modulation of Stoichiometry, Morphology and Composition of Transition Metal Oxide Nanostructures through Hot Wire Chemical Vapor Deposition. *J. Mater. Res.* **2016**, *31*, 17.

(31) Chakrapani, V.; Thangala, J.; Sunkara, M. K. WO$_3$ and W$_2$N nanowire arrays for photoelectrochemical hydrogen production. *Int. J. Hydrogen Energy* **2009**, *34* (22), 9050−9059.

(32) Thangala, J.; Chen, Z.; Chin, A.; Ning, C.-Z.; Sunkara, M. K. Phase Transformation Studies of Metal Oxide Nanowires. *Cryst. Growth Des.* **2009**, *9* (7), 3177−3182.

(33) Lide, D. R. *CRC Handbook of Chemistry and Physics*; Chemical Rubber Co.: Boca Raton, FL, 2003.

(34) Granqvist, C. G. Electrochromic oxides: a bandstructure approach. *Sol. Energy Mater. Sol. Cells* **1994**, *32* (4), 369−382.

(35) Passerini, S.; Scrosati, B.; Gorenstein, A. The Intercalation of Lithium in Nickel Oxide and Its Electrochromic Properties. *J. Electrochem. Soc.* **1990**, *137* (10), 3297−3300.

(36) Boschloo, G.; Hagfeldt, A. Spectroelectrochemistry of Nano-structured NiO. *J. Phys. Chem. B* **2001**, *105* (15), 3039−3044.

(37) Ge, C.; Jin, K.-J.; Gu, L.; Peng, L.-C.; Hu, Y.-S.; Guo, H.-Z.; Shi, H.-F.; Li, J.-K.; Wang, J.-O.; Guo, X.-X.; Wang, C.; He, M.; Lu, H.-B.; Yang, G.-Z. Metal−Insulator Transition Induced by Oxygen Vacancies from Electrochemical Reaction in Ionic Liquid-Gated Manganite Films. *Adv. Mater. Interfaces* **2015**, *2* (17), 1500407.

(38) Ji, H.; Wei, J.; Natelson, D. Modulation of the Electrical Properties of VO$_2$ Nanobeams Using an Ionic Liquid as a Gating Medium. *Nano Lett.* **2012**, *12* (6), 2988−2992.

(39) Asanuma, S.; Xiang, P.-H.; Yamada, H.; Sato, H.; Inoue, I. H.; Akoh, H.; Sawa, A.; Ueno, K.; Shimotani, H.; Yuan, H.; Kawasaki, M.; Iwasa, Y. Tuning of the metal-insulator transition in electrolyte-gated NdNiO3 thin films. *Appl. Phys. Lett.* **2010**, *97* (14), 142110.

(40) Pizzini, S.; Morlotti, R. Thermodynamic and Transport Properties of Stoichiometric and Nonstoichiometric Nickel Oxide. *J. Electrochem. Soc.* **1967**, *114* (11), 1179−1189.

(41) Grosvenor, A. P.; Biesinger, M. C.; Smart, R. S. C.; McIntyre, N. S. New interpretations of XPS spectra of nickel metal and oxides. *Surf. Sci.* **2006**, *600* (9), 1771−1779.

(42) Biesinger, M. C.; Payne, B. P.; Lau, L. W. M.; Gerson, A.; Smart, R. S. C. X-ray photoelectron spectroscopic chemical state quantification of mixed nickel metal, oxide and hydroxide systems. *Surf. Interface Anal.* **2009**, *41* (4), 324−332.

(43) Oswald, S.; Brückner, W. XPS depth profile analysis of non-stoichiometric NiO films. *Surf. Interface Anal.* **2004**, *36* (1), 17−22.

(44) Gupta, R. P.; Sen, S. K. Calculation of multiplet structure of core p-vacancy levels. *Phys. Rev. B* **1974**, *10* (1), 71−77.

(45) Gupta, R. P.; Sen, S. K. Calculation of multiplet structure of core p -vacancy levels. II. *Phys. Rev. B* **1975**, *12* (1), 15−19.

(46) Rajam, K.; Rajagopalan, S.; Hegde, M.; Viswanathan, B. Characterization of electroless nickel by esca. *Mater. Chem. Phys.* **1991**, *27* (2), 141−154.

(47) Peng, H. Y.; Li, Y. F.; Lin, W. N.; Wang, Y. Z.; Gao, X. Y.; Wu, T. Deterministic conversion between memory and threshold resistive switching via tuning the strong electron correlation. *Sci. Rep.* **2012**, *2*, 442.

(48) Hubbard, J. Electron Correlations in Narrow Energy Bands. III. An Improved Solution. *Proc. R. Soc. London, Ser. A* **1964**, *281* (1386), 401−419.

(49) Zaanen, J.; Sawatzky, G. A.; Allen, J. W. Band gaps and electronic structure of transition-metal compounds. *Phys. Rev. Lett.* **1985**, *55* (4), 418−421.

(50) Tomellini, M. X-ray photoelectron spectra of defective nickel oxide. *J. Chem. Soc., Faraday Trans. 1* **1988**, *84* (10), 3501−3510.

(51) Svensson, J. S. E. M.; Granqvist, C. G. Electrochromic hydrated nickel oxide coatings for energy efficient windows: Optical properties and coloration mechanism. *Appl. Phys. Lett.* **1986**, *49* (23), 1566−1568.

(52) Greiner, M. T.; Helander, M. G.; Tang, W.-M.; Wang, Z.-B.; Qiu, J.; Lu, Z.-H. Universal energy-level alignment of molecules on metal oxides. *Nat. Mater.* **2011**, *11* (1), 76−81.

(53) Yoshimura, T. Oscillator strength of small-polaron absorption in WOx ($x \leq 3$) electrochromic thin films. *J. Appl. Phys.* **1985**, *57* (3), 911−919.

(54) Yao, J.; Koski, K. J.; Luo, W.; Cha, J. J.; Hu, L.; Kong, D.; Narasimhan, V. K.; Huo, K.; Cui, Y. Optical transmission enhacement through chemically tuned two-dimensional bismuth chalcogenide nanoplates. *Nat. Commun.* **2014**, *5*, 5670.

(55) Bao, W.; Wan, J.; Han, X.; Cai, X.; Zhu, H.; Kim, D.; Ma, D.; Xu, Y.; Munday, J. N.; Drew, H. D.; Fuhrer, M. S.; Hu, L. Approaching the limits of transparency and conductivity in graphitic materials through lithium intercalation. *Nat. Commun.* **2014**, *5*, 4224.

(56) Xiong, F.; Wang, H.; Liu, X.; Sun, J.; Brongersma, M.; Pop, E.; Cui, Y. Li Intercalation in MoS$_2$: In Situ Observation of Its Dynamics and Tuning Optical and Electrical Properties. *Nano Lett.* **2015**, *15* (10), 6777−6784.